Aeroacoustic Interaction Effects of Adjacent Propellers in Forward Flight

Zarri, A.; Koutsoukos, P.A.; Avallone, F.; de Prenter, Frits; Ragni, D.; Casalino, D.

DOI
10.2514/6.2023-4489

Publication date
2023

Document Version
Final published version

Published in
AIAA AVIATION 2023 Forum

AIAA AVIATION Forum
12-16 June 2023, San Diego, CA and Online
AIAA AVIATION 2023 Forum

10.2514/6.2023-4489

Aeroacoustic Interaction Effects of Adjacent Propellers in Forward Flight

Alessandro Zarri *
von Karman Institute for Fluid Dynamics, 1640 Rhode-St-Genèse, Belgium

Alexandros Koutsoukos †
Delft University of Technology, 2629 HS Delft, The Netherlands

Francesco Avallone ‡
Politecnico di Torino, 10129 Torino, Italy

Frits de Prenter, § Daniele Ragni ¶, and Damiano Casalino ‖
Delft University of Technology, 2629 HS Delft, The Netherlands

Distributed electric propulsion systems are an emerging technology with the potential of revolutionizing the design and performance of aircraft. When propellers are located in close proximity, they can be subjected to aerodynamic interactions, which affect the far-field noise. In this paper, we study an array of three co-rotating and adjacent propellers to describe both the aerodynamic and acoustic installation effects. A scale-resolving CFD simulation based on the Lattice-Boltzmann/Very-Large-Eddy-Simulation method is used to solve the flow field around the propellers. An acoustic analogy integral approach calculates the far-field noise. Findings show that the helical vortical structures, generated at the tip of each blade undergo a flow deformation at the location of interaction. This causes the loading of each blade to vary during the rotation. Consequently, the unsteady loading noise becomes a dominant noise generation mechanism, driving the noise levels and directivity. It is also shown that introducing a non-zero relative phase angle between the propellers results in a reduction of the unsteady thrust, leading to a mitigation of the unsteady-loading tonal components along the rotation axis. Additionally, the relative phase angle causes constructive/destructive acoustic interference, as demonstrated by analyzing the noise emitted simultaneously by the three propellers.

I. Introduction

New aircraft propulsion systems are being investigated in the aeronautical community to meet future objectives for low noise and pollutant emissions [1]. Due to the advantage of separating the location where the energy is generated or stored, from where it is converted in momentum applied to the flow, the Distributed Electric Propulsion (DEP) concept has the potential to increase aircraft propulsive efficiency and reduce the community noise [2]. Thrust is generated through arrays of propellers distributed along the wingspan [3–5]. Benefits associated with distributing propellers side-by-side ahead or above the wing are the spanwise lift augmentation [6], and the increase of low-speed performance [7]. In addition, because the propellers are driven by electric motors, DEP aircraft have the potential to be much more energy sustainable, paving the way for futuristic designs such as the Helios Prototype Flying Wing by NASA [8].

When propellers are adjacent to each other, complex aerodynamic and acoustic interactions occur, which ought to be considered in the development of new vehicle concepts. Studies in the literature involving multiple propellers have mainly focused on the hover condition. It is shown that proximity between propellers causes, depending on configuration, a detrimental effect on thrust generation, corresponding to a loss of up to 8% [9, 10]. The higher percentages appear

*Postdoctoral Researcher, Department of Environmental and Applied Fluid Dynamics, alessandro.zarri@vki.ac.be.
†Researcher, Department of Flow Physics and Technology, p.alex.koutsoukos@gmail.com.
‡Assistant Professor, Department of Mechanical and Aerospace Engineering, francesco.avallone@polito.it.
§Assistant Professor, Department of Flow Physics and Technology, f.deprenter@tudelft.nl.
¶Associate Professor, Department of Flow Physics and Technology, d.ragni@tudelft.nl.
‖Professor, Department of Flow Physics and Technology, d.casalino@tudelft.nl.

especially for hovering conditions. At the same time, an important increase in the aerodynamic blade load oscillations at small distances between the propellers is observed [11, 12], yielding vibrations and noise radiations. These studies show that when rotors operate in close proximity, the evolution of slipstreams is impacted. In particular, their helical path is deformed due to the interaction between the tip vortices of neighboring rotors, which distorts their trajectory causing them to merge and break-up.

A recent study by de Vries *et al.* [13], involving an array of three adjacent propellers, focused on the forward-flight conditions. The authors observed an efficiency loss with respect to the isolated-propeller case of 1.5% for a tip clearance equal to 4% of the propeller radius. Furthermore, it was shown that the slipstreams generated by each propeller do not merge thus generating a high-momentum flow region, as previously assumed; as a matter of fact, the time-averaged evolution of the slipstreams was not drastically affected when propellers were located close to each other. Consequently, each slipstream could be easily distinguished at downstream locations where a wing could be installed. This may be attributed to the fact that, in forward flight, the dominance of inertia forces over viscous ones would result in less intense viscous interactions than in hover, preventing the slipstreams to deform and merge.

The present research is intended to complement the experimental time-averaged study by de Vries *et al.* [13], by considering the same array of propellers in forward-flight conditions and by performing high-fidelity simulations to gain insight into the unsteady flow behaviour. The interest of this article is to investigate the tip-on-tip interaction effects by looking at the unsteady formation, evolution, and deformation of the slipstream when subjected to the presence of adjacent propellers. The first objective is to clarify whether there is a link between the slipstream's deformation, blade unsteady load generation, and far-field noise. This is motivated by the fact that it has been shown that by decreasing the separation distance among propellers, the emitted sound increases in both tonal and broadband components [11]. The tip-on-tip interaction would induce non-uniform inflow conditions leading to periodic loads that radiate tonal noise [14]. Broadband noise related to turbulence interactions is also enhanced, by both the trailing-edge scattering of the turbulent boundary layer [15] and the mixing of tip vortices causing eddy dissipation, yielding random fluctuations on the blades [9]. Hence, we intend to quantify the noise generation and directivity variations caused by the aerodynamic installation of the adjacent three propellers with respect to the isolated-propeller case. We will focus in particular on tonal noise, which is the one perceived by the human ear as more annoying [16].

The second objective of this work is to investigate the effect of the relative phase angle between the three propellers. Indeed, by synchronizing the azimuthal position of two or more rotors, it is possible to achieve partial cancellation of sound emissions in some directions due to the destructive inference [17]. By accurately selecting the phase angle and with a maximum nominal rotational speed deviation of less than 0.5%, Pascioni *et al.* [18] experimentally obtained a decrease of 6 dB at the rotor's Blade Passing Frequency (BPF). Zhou and Fattah [19] similarly observed that the phase angle between two propellers can affect their sound emissions up to 10 dB. While the phase angle can be used as an active noise reduction means that can lead to benefits of 17 dB at a given listener location [20], the effect of unsteady aerodynamic interactions remains unexplored in the literature, especially in forward-flight conditions. In fact, in addition to constructive and/or destructive acoustic interference, the different relative positioning between the blades affects the local unsteady loading at the blade tip, thus the evolution of slipstreams, and thus the acoustic emissions [13]. We aim at quantifying the latter by providing a physical understanding of why sound radiation is being modified and whether this depends solely on acoustic interference or whether the aerodynamic sources of sound are considerably altered by changes in the phase angle. Simulations based on a Lattice-Boltzmann Method hybridized with a Very Large Eddy Simulation (LBM/VLES) model for turbulence are computed in this paper and coupled with an acoustic solver based on Farassat's formulation 1A of the FW-H's equation to predict both broadband emissions and the tonal thickness and loading noise. This simulation technique has previously been successfully applied to deal with propellers operating in similar Reynolds and Mach numbers [21–23]. This work is organized as follows: in Section II, the numerical approach selected for calculating the flow-field is introduced, followed by a description of the acoustic solver. Section III describes the computational setup with the three adjacent propellers. In Section IV, the aerodynamic simulation is validated against experimental measurements, whereas the acoustic results are compared with the ones obtained employing a low-fidelity noise-prediction methodology. The flow developing around the isolated- and distributed-propulsion cases is studied in Section V. The acoustic results are described in Section VI. Finally, Section VII summarizes our findings and outlines future steps.

II. Computational method

The commercial CFD/CAA software SIMULIA PowerFLOW®, version 6-2021-R2, is used to solve the flow around the propellers. It solves the discrete LB equation for the distribution function $f(\boldsymbol{x}, \boldsymbol{v}, t)$, which represents the probability

density of particles with velocity $\boldsymbol{v}$ at location $\boldsymbol{x}$ and time t. A D3Q19 stencil, which utilizes 19 discrete velocities in the 3 spatial dimensions, is considered, together with a regularized collision operator based on the Bhatnagar-Gross-Krook (BGK) collision model [24]. Hydrodynamic flow quantities, such as flow density and velocity, can be determined through discrete integration of the discrete distribution function [25]. For high-subsonic Mach-number simulations, e.g, flows with local Mach number greater or near 0.5, as in the present case, the LB solver is coupled with the solution of an energy conservation equation solved through a Lax-Wendroff finite difference scheme on the Cartesian LB mesh [26].

A Cartesian grid with cubic volumetric elements (voxels) is used to solve the LB equations, while planar surface elements (surfels) are used to discretize the surfaces of solid bodies within each voxel that intersects the wall geometry. The no-slip and slip wall boundary conditions are recovered by exploiting a boundary system based on a particle bounce-back process and a specular reflection process, respectively [27].

The solver employs a VLES approach to model the effects of the unresolved scales of turbulence. A two-equation transport model based on the k-ϵ renormalization group theory [28] is used to compute the turbulent relaxation time associated with time scales of the resolved sheared flow field [29]. In a turbulent flow, this relaxation time drives the collision process of the kinematic model in which the equilibrium state corresponds to the local level of turbulent kinetic energy.

To reduce the computational cost, a pressure-gradient extended wall model is used to approximate the no-slip boundary condition on solid walls. This model is based on the extension of the generalized law-of-the-wall model to take into account the effect of the pressure gradient.

The far-field noise is computed *via* an impermeable FW-H formulation, known as Farassat's Formulation 1A [30], solved in forward time [31], and implemented within the post-processing software SIMULIA PowerACOUSTICS®. It involves distributions of acoustic monopoles and dipoles calculated by means of surface integrals on solid surfaces, accounting for the thickness and loading noise, respectively. The quadrupolar term related to non-linear effects in the volume surrounding the integration surface is neglected. In fact, this term accounts for sound sources generated by shock waves, turbulence mixing, and non-linear propagation effects, which are of minor importance for propellers operating at low blade-tip Mach number [32, 33].

III. Computational setup

The computational test case is based on the experiments performed by de Vries *et al.* [13], involving a setup with three adjacent propellers, as shown in Figure 1(a)). These are known as TUD-XPROP-S propellers, featuring six blades and a diameter $D = 0.2032$ m, whose geometry was made available by the Delft University of Technology [13]. The pitch angle is equal to 30° at 70% of the radius ($r/R = 0.7$, where r is the local radial location and R is the propeller radius), whereas the root chord length of the blades is $c_r = 16.287$ mm. More details concerning the geometry of the propeller, such as the pitch angle and chord distributions along the blade span are given in Ref. [13].

While the spinner and the blade geometries are exactly replicated from the experiments, the wind-tunnel test section is not included in the computational domain; similarly, the supports that hold the nacelles in place during the measurements are not included. The nacelles are designed with a length corresponding to $3.7R$ and with a tapered termination to minimize any possible disturbance to the flow field around the rotors.

Three identical propellers are distributed along the Y-axis, with tip clearance of $\delta = 0.02D = 4.064$ mm, as shown in Figure 1(b). In the same figure the Global Reference System (GRS) (X, Y, Z) is also introduced. Figure 1(a) shows a configuration with a co-rotating direction of the propellers (anticlockwise) and a relative phase angle of $\Delta\phi = 15°$. In order to investigate the influence of the relative phase angle on the aerodynamic and acoustic performance, an additional configuration with $\Delta\phi = 0°$ is investigated.

The propellers are operated at free-stream velocity $V_\infty = 30$ m s^{-1}, directed along the X-axis, and at an advance ratio $J = V_\infty/(nD) = 0.8$, where n is the number of rotations per second. The Mach number at the tip is equal to 0.357 and the Reynolds number at the tip is 5.66×10^4, given that the chord at the tip is equal to 6.8 mm. The free-stream static pressure and temperature are $p_\infty = 101330$ Pa and $T_\infty = 288.15$ K. The inlet turbulence intensity is set to a value of 0.04%, similar to the experiments. The rotation time is equal to $T_{rot} = 5.41867 \times 10^{-3}$ s.

The simulation volume, depicted in Figure 1(a), is a cubic box whose side faces are placed $64D$ away from the GRS origin. To prevent acoustic reflections at the outer boundary, an acoustic sponge, i.e. an anechoic outer layer, is defined by two concentric spheres of radius $8D$ and $30D$, respectively, centred at the GRS origin [21, 34]. In this region, the viscosity increases up to a constant value at radial locations larger than $30D$. A total of 15 Variable Resolution (VR) regions are employed; the change in resolution between adjacent VR regions is equal to 2. The first 8 VRs are defined as the boxes shown in Figure 1(a) (the simulation volume being set at VR0), where the correct scaled dimensions are

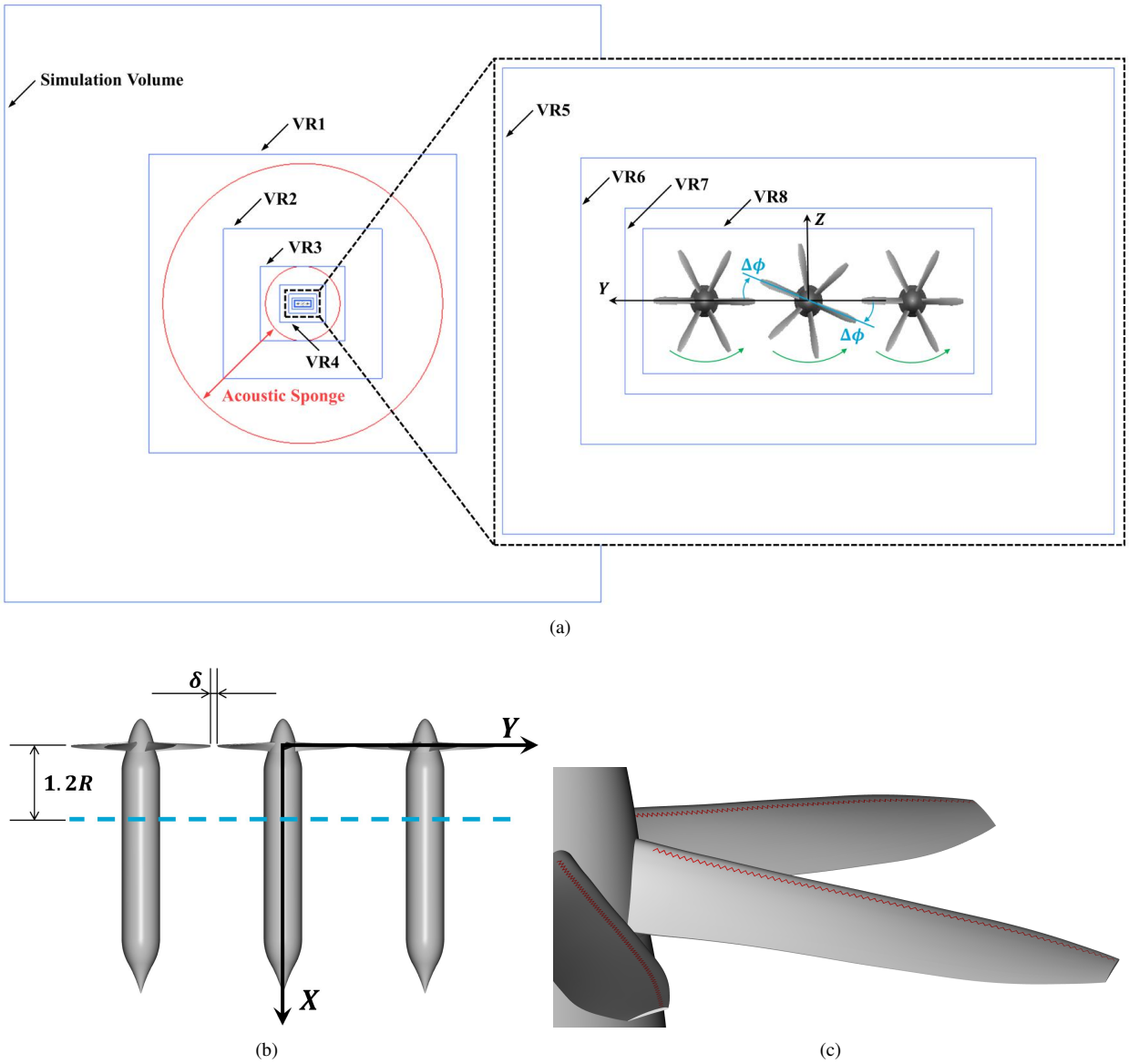

Fig. 1 (a) Front view of the computational domain with the Variable Resolution (VR) mesh regions and the global reference frame. (b) Top view of the three adjacent propellers with wake survey plane location in a dashed line. (c) Close-up on the zig-zag trip applied on the blades.

reported and where the refinement level is increased moving toward the GRS origin. In Figure 2(a), three volumes of revolution defining the Local Reference Frame (LRF) of each propeller are indicated with solid lines. Each of the grids contained within these regions slides with respect to the outer stationary grid. Within the revolution volumes, a refinement (VR9) is applied. Cylindrical hollow refinements set to VR9 can also be observed: these are used to better discretize the regions enveloping the slipstream helical paths. VR10 is applied around the blade and spinner surfaces and to ring refinement regions following the blade tip motion, as illustrated in Figure 2(b). The latter approach is needed to allow a minimum of 4 voxels to discretize the non-rotating gaps between the tips of the blades. VR10, VR11, and VR12 are applied on the blade surfaces, where a fine discretization is needed to capture the surface pressure fluctuations. The nacelles are enveloped by VR9. The finest VR13 and VR14 envelope the zig-zag trip device that is located at 10% from the blade leading edge (see it in Figure 1(c)). This is done to discretize the trip thickness with about three voxels, as suggested in Ref. [35].

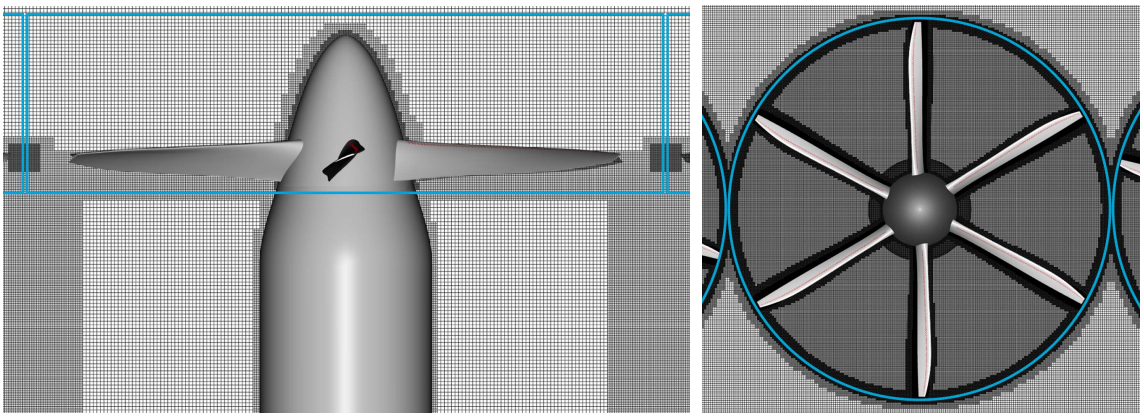

(a) (b)

Fig. 2 Near-body grid size with volumes of revolution enclosed by a solid line: top view (a) and front view (b).

A physical zig-zag trip is applied on the blade suction side to force turbulent boundary-layer transition and cause the VLES to switch from a modeled- to a resolved-scale modality. This solution, adopted in previous numerical simulations [21, 36], is selected to minimize the computational cost of the simulations without neglecting the contribution of turbulent boundary layer trailing-edge noise for future studies. As a matter of fact, at the Reynolds number ($Re \approx 10^4$) at which experiments have been carried out, we might expect the appearance of a laminar separation bubble followed by turbulent reattachment [37]. This causes a broadband hump in the far-field spectra at frequencies higher than the BPF. This behaviour can be reproduced numerically without a physical zig-zag trip, as it was shown by Romani *et al.* [22], by increasing resolution such that the surface $y+$ is smaller than 15 at each point on the blades' surface. However, for the three-propellers setup, the associated computational cost is too high and the physical zig-zag trip solution has been preferred to still account for all the relevant sources of noise. The zig-zag trip is built using the Opty∂B toolkit, embedded in PowerFLOW rotor noise workflow [35], and it features a chordwise amplitude of $0.05c_r$, a spanwise length between two subsequent zig-zag peaks of $0.1c_r$.

For the finest grid case, a total of about 225.5 million voxels are used to discretize the case, with a resolution at VR14 of 900 voxels per characteristic length (c_r). This leads to the smallest voxel size of 1.79445×10^{-5} m. The isolated-propeller case involves the same setup and characteristics as the distributed one described above, with about one-third of the total voxel count.

The acoustic data is sampled at 33.218 kHz on the solid FW-H integration surfaces, corresponding to the propeller blades. This is done to achieve a time discretization up to the tenth BPF harmonic multiplied by a Nyquist factor of 3 (to avoid aliasing artifacts). The Power Spectral Density (PSD) is computed with one Welch block, filtered by a Hanning window, corresponding to a bandwidth of $\Delta f_r = 91.28$ Hz. The PSD of the far-field noise as a function of the frequency f is computed as:

$$S_{pp}(f) = 10 \log_{10} \frac{\mathrm{PSD(f)}}{p_{ref}^2},$$

where $p_{ref} = 20\,\mu$Pa is the reference pressure. The Sound Pressure Level (SPL) is defined as:

$$L_p(f) = 10 \log_{10} \frac{\Delta f_r \mathrm{PSD(f)}}{p_{ref}^2},$$

in order to obtain acoustic decibels as output.

IV. Validation and comparison with low-order acoustic methodologies

Figure 3(a) shows the grid convergence study for the isolated-propeller case. The value of the thrust coefficient is defined as $T_c = T/(q_\infty \pi R^2)$, where T is the thrust and q_∞ is the upstream undisturbed dynamic pressure.

In the coarser case, all VRs greater than VR8 are turned off, while for the mid-resolution case, those above VR11 are turned off. As can be seen, the trend gets closer to the measurements [13], until a difference of 0.9% is achieved

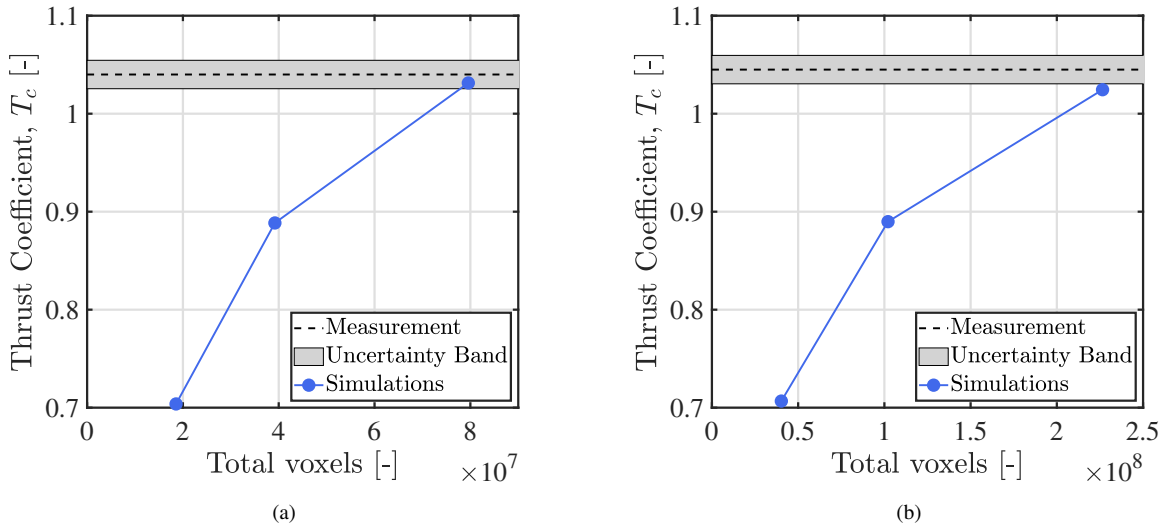

Fig. 3 Convergence of the thrust coefficient against the total number of voxels for the isolated propeller (a) and the middle propeller of the $\Delta\phi = 15°$ configuration (b).

with the finest mesh. The latter is then used to conduct the following analyses. The same grid refinement approach is conducted for the DP simulations. In particular, Figure 3(b) shows the case with $\Delta\phi = 15°$, in which a difference of 2.0% is obtained for the thrust generated by the central propeller. The time-averaged thrust predictions achieved at these accuracy levels are deemed satisfactory for concluding that the grids under consideration are sufficiently refined to capture the investigated aeroacoustic mechanisms.

Since the acoustic data measured in Ref. [13] were not obtained in an anechoic environment, a direct comparison is not possible. In fact, the simulations, as described in Section III, do not contain acoustic reflections due to the wind-tunnel geometry. Consequently, we compare the simulated SPL against the one obtained following the low-fidelity methodology present within the Opty∂B toolkit, based on a Blade Element Momentum Theory (BEMT) model to compute the radial distribution of forces [35], and a time-domain FW-H formulation based on a compact dipole and compact monopole formulation [38].

Figure 4(a) shows the directivity of tonal sound at the first BPF calculated, by means of the BEMT/FW-H approach, in the XY plane, namely the one containing the axis of rotation and perpendicular to the plane of the rotor. In this work, L_p is always calculated on this plane and at $10D$ from the GRS origin on this plane, unless differently specified. According to propeller noise theory [32], steady-loading noise and thickness noise dominate the sound emissions generated by an isolated rotor for observers located in the plane of the rotor. Indeed, one can see the characteristic vertical lobe shape which reaches a maximum for observers placed in this plane. In contrast, the sound directivity reaches a minimum for listeners placed in the direction of the axis of rotation. Notice how the LBM/VLES simulation of the isolated case reports the vertical lobe shape with a deviation of less than 2 dB on the vertical axis. This occurs for both observers placed in the XY plane and those in the XZ plane. This small discrepancy is attributed to unsteady loading effects that are absent in the BEMT + FW-H computation. Since the isolated case is axisymmetric, these two curves should overlap perfectly in both planes. However, on the horizontal axis, in the angular ranges between 330° and 30° and between 150° and 210°, two different trends of L_p directivity are observed. This is because in such directions the contribution of steady loading noise and thickness noise is very low. What remains is due to random acoustic pressure fluctuations of very small magnitude (we are around and below 20 dB). In Figure 4(b), we show the directivity of the calculated SPL for the DP case with $\Delta\phi = 15°$ at the first BPF. This figure depicts the sound emitted by the middle propeller, but it can similarly be shown that even taking into account the contribution of the two adjacent propellers, the loading noise is always far greater than the thickness noise in each direction (minimum difference of 4.4 dB up to 67 dB in the upstream direction).

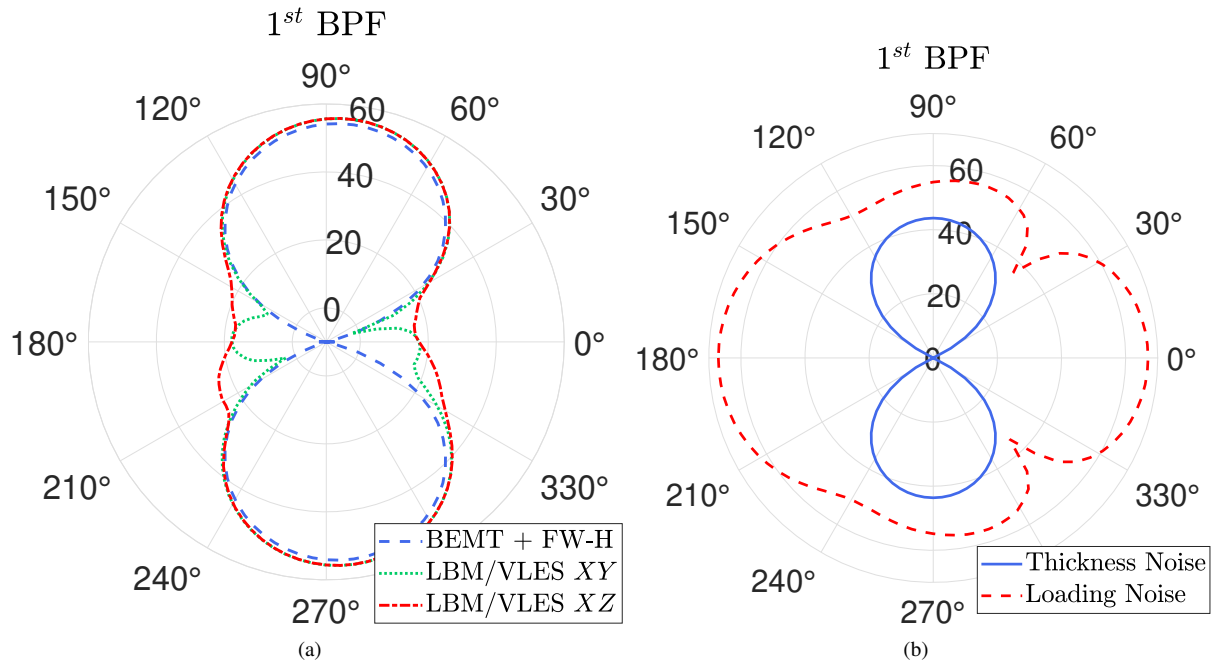

Fig. 4 Far-field sound L_p at the first BPF. In (a), this is computed for the isolated-propeller simulation in XY and XZ planes against the one computed *via* BEMT+FW-H low-fidelity approach. In (b), the contribution of the thickness noise against loading noise is represented for the middle propeller of the $\Delta\phi = 15°$ configuration.

V. Flow-field analysis

In Figure 5(a), the slipstream development for the isolated-propeller case at a given time instant is reported by means of the λ_2 criterion, computed with a value of $\lambda_2 = -2 \times 10^6$ 1/s^2. It can be seen that the vortical structures follow a helical path starting from the blade tip and evolving essentially undisturbed downstream of the rotor. Referring to the DP case with $\Delta\phi = 15°$ in Figure 5(b), we notice a similar behavior of each slipstream, which do not merge together or break-up, in agreement with the experimental results [13]. Nevertheless, we do observe that the proximity between the rotors induces a deformation of the vortex structures that become progressively more pronounced moving downstream of the rotor. This interaction is due to the circulations of the vortical structures mutually influencing their trajectories and that of the structures adjacent to them through the generation of an induced-velocity field.

In Figure 6(a), we report the thrust produced by the blades of the simulated propellers as a function of the physical time t normalized by the rotation time T_{rot}. We notice how the isolated propeller generates a relatively constant thrust profile with small fluctuations from the mean value possibly caused by its own wake development. Differently, propellers belonging to the DP case (for instance, the $\Delta\phi = 15°$ case reported in the figure) show greater oscillations from their mean value. In particular, the side propellers (see Figure 1(b)), present peak-to-peak oscillations of about 0.4% from the mean value, while the middle one exhibits fluctuations of about twice as much. This indicates that the fluctuations are caused by the aerodynamic interactions between the propellers, since the middle one interacts on both sides. It is thus shown that the tip-on-tip interaction increases the unsteadiness of the thrust generated by the blades, anticipating an augmentation of noise production, as reported in Section VI. Moreover, consistently with the experimental findings [13], we confirm that the impact of the angle $\Delta\phi$ on time-averaged thrust, and hence on aerodynamic performance, is negligible when compared to the isolated-propeller case, as it was consistently less than 0.75% across all analyzed cases. The thrust of the propeller in the middle for the DP configurations is reported in Figure 6(b). The thrust profile is modulated by a sinusoidal pattern that has a periodicity of six times the period of rotation. This is clearly due to the interaction with the blades of adjacent propellers. Furthermore, we may notice the expected temporal phase shift corresponding to 15° compared with the case with $\Delta\phi = 0°$. However, we further remark that the average peak-to-peak ratio for the case with $\Delta\phi = 15°$ is only 0.60%. This means the evolution of the slipstreams affects the magnitude of the tip-on-tip interaction, which becomes a function of the relative phase angle $\Delta\phi$.

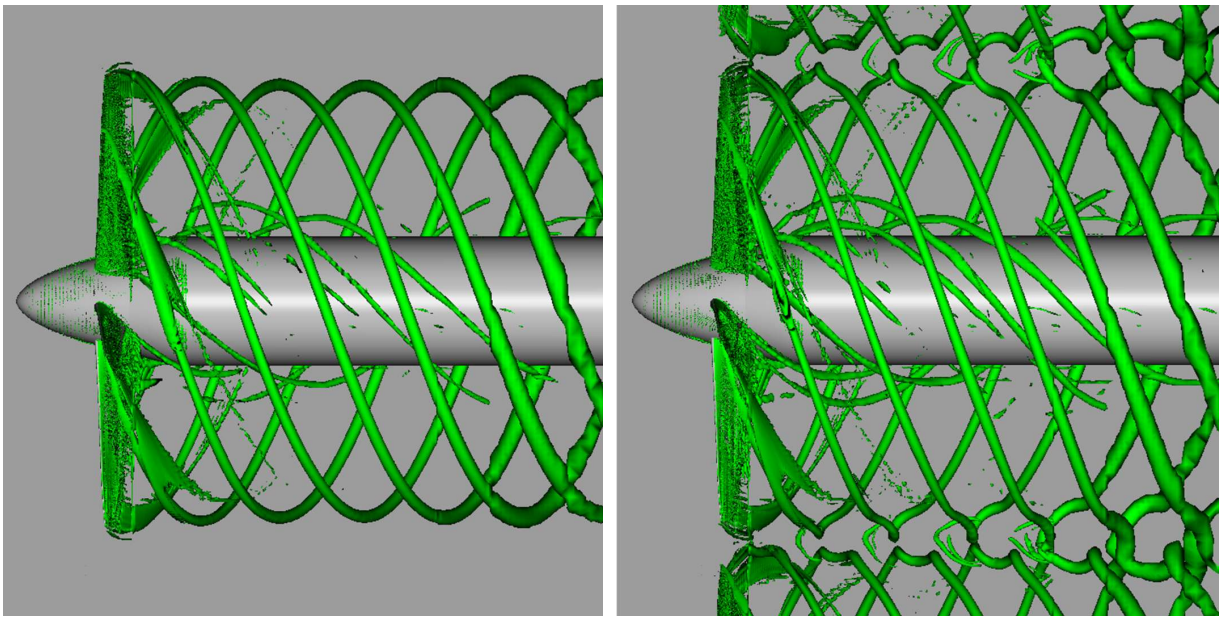

(a) (b)

Fig. 5 Isosurface computed through the $\lambda 2$ criterion with a value of $\lambda_2 = -2 \times 10^6$ $1/s^2$: isolated-propeller case (a), distributed-propeller case $\Delta\phi = 15°$ (b).

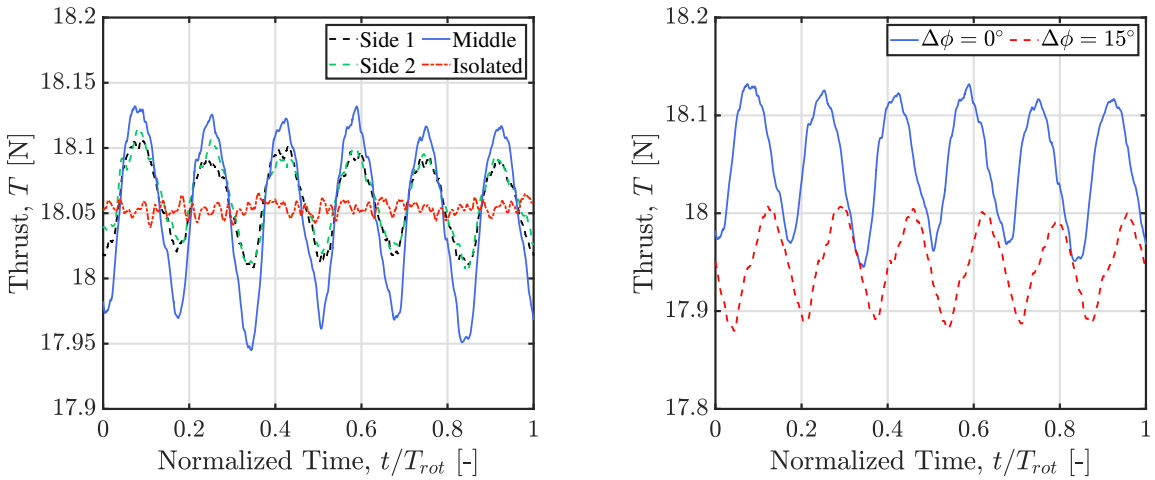

(a) (b)

Fig. 6 (a) Thrust values produced by the blades of the propellers of the distributed configuration (Side 1, Side 2, and Middle) and of the single propeller case (Isolated). (b) Thrust values produced by the blades of the middle propellers for the two analyzed DP cases.

In Figure 7(a), the time-averaged velocity magnitude of the isolated propeller is reported. It is shown in a plane parallel to the rotational plane, placed $1.2R$ downstream of the propeller as indicated in Figure 1(b). This corresponds to a typical distance at which a wing would be installed, as stated in Ref. [13]. We observe that the flow field is uniform along the azimuthal direction and symmetric with respect to the propeller axis. In contrast, when we refer to the distributed case with $\Delta\phi = 0°$ given in Figure 7(b), we notice that at the interaction zones between the tips, there is a time-averaged flow-field deformation. Therefore, the proximity between the propellers induces a time-averaged deformation on the wake that propagates to a typical distance at which a wing would be located, inducing non-uniform aerodynamic loads on the wing.

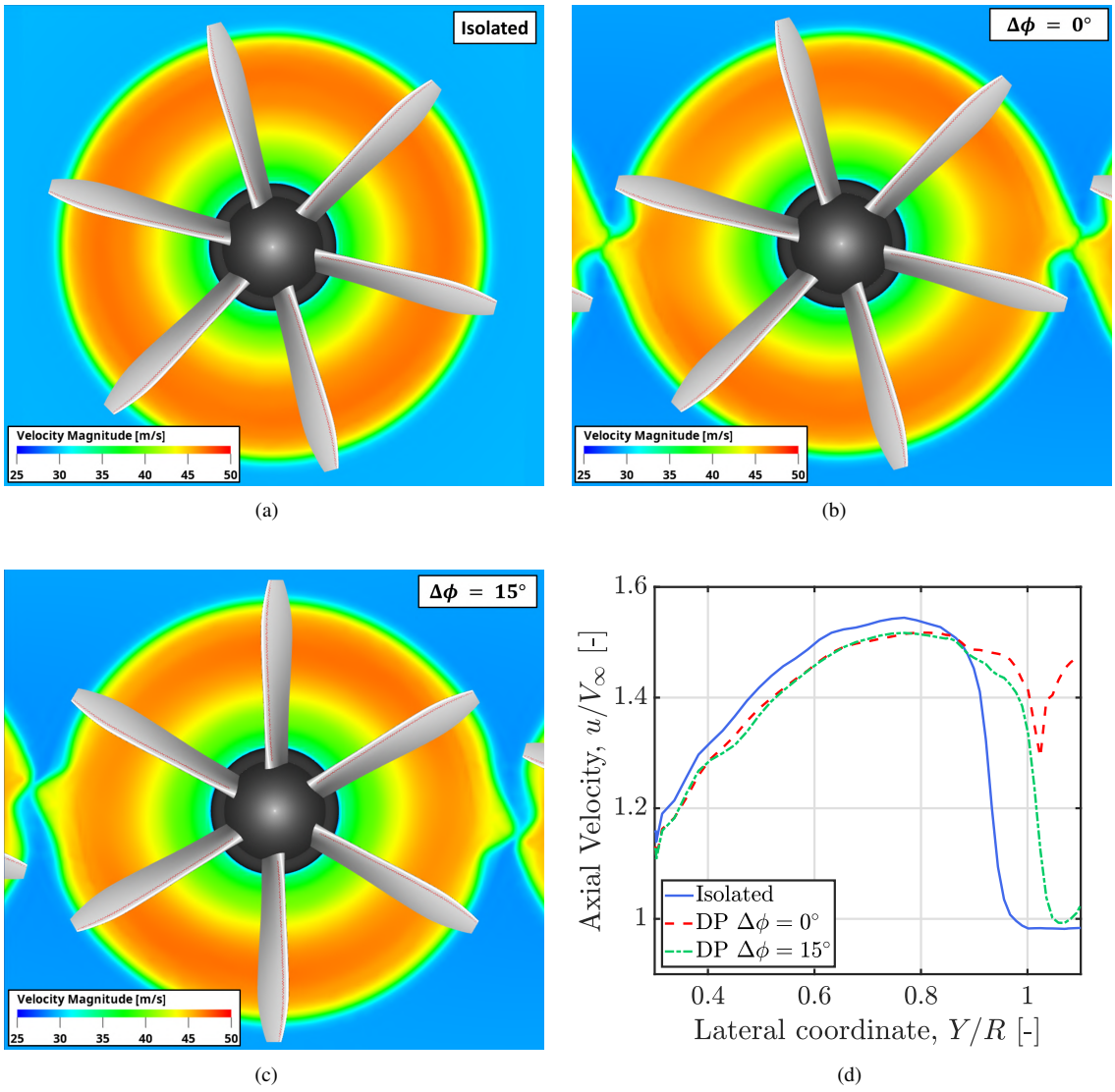

Fig. 7 Time-averaged velocity magnitude at the plane location depicted in Figure 1(b): isolated propeller (a), distributed configurations with $\Delta\phi = 0°$(b), and $\Delta\phi = 15°$ (c). Axial velocity comparison of the 3 analyzed cases at the plane location defined in Figure 1(b) (d).

We observe that the distributed cases with $\Delta\phi = 15°$, shown in Figures 7(c), also exhibit deformation of the slipstreams in the region between propellers. However, in the former case, the flow of the middle propeller bends outward first when the blades approach the adjacent ones, whereas in the latter case, the flow bends firstly inward. Hence, we understand that the relative phase angle $\Delta\phi$ between the propellers has an effect not only on the slipstream instantaneous evolution, but also on the time-averaged flow field. Qualitatively similar time-averaged deformations have also been observed experimentally in Ref [13], albeit with differences due to the choice of the relative phase angle between the blades and to the different advance ratio.

The computed axial velocities along the positive direction of the Y axis and at $X = 1.2R$ and $Z = 0$ are shown in Figure 7(d). We observe that the isolated-propeller case reaches the maximum of $u/V_\infty = 1.54$ at a distance $Y/R = 0.77$, followed by a rapid decrease toward undisturbed flow conditions at the blade tip end. In contrast, both distributed-propulsion cases exhibit outward wake widening due to the mutual induction velocity between blade tip vortices, yielding a maximum of $u/V_\infty = 1.51$ at a distance of $Y/R = 0.80$. This effect is also found in the experimental measurements in Ref. [13] and is responsible for the general widening of the wake in the Y-axis direction, losing the

circular symmetry proper to the isolated propeller. We also remark that the case with $\Delta\phi = 0°$ shows symmetry in the evolution of the axial velocity at $Y/R = 1.04$, i.e., exactly half the distance between adjacent propellers. In contrast, the case with $\Delta\phi = 15°$, exhibits greater widening than the previous case, as the point of minimum axial velocity is reached at $Y/R = 1.06$. This is due to the phase shift (exactly 15°) of the tip vortex cores produced in this case, which maintain this phase difference during their downstream evolution.

To investigate how the tip-on-tip interaction impacts the azimuthal and radial distribution of thrust, we calculate the difference between the thrust coefficient of the DP case with $\Delta\phi = 15°$ versus that of the isolated case ($\Delta T_c = T_{c_{\Delta\phi=15°}} - T_{c_{iso}}$) in the rotor plane. The blade is divided into 100 spanwise segments on which ΔT_c is computed. Figure 8(a) illustrates that for the side propeller (the one located on the positive direction of the Y-axis in Figure 1(b))

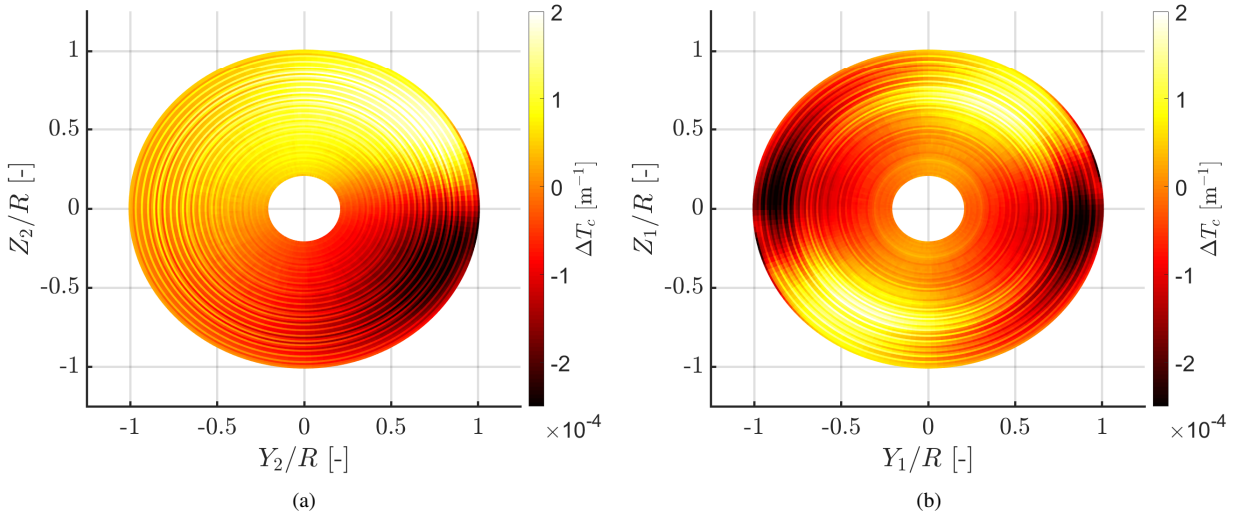

Fig. 8 Thrust coefficient distribution difference (ΔT_c) between the distributed configuration with $\Delta\phi = 15°$ and the isolated propeller. Side1 propeller depicted in (a), Middle propeller depicted in (b).

the thrust coefficient's azimuthally uniform distribution is disrupted. This happens when the blades come closer to the middle propeller: in the approaching phase, the thrust decreases until it reaches the minimal distance from the middle-propeller blades. After that, the thrust increases again. This process is repeated twice in one revolution for the middle propeller, as shown in Figure 8(b), namely when the blades approach and retreat the side propellers. One notable aspect is that the alterations in thrust occur close to the blade tip, with the highest thrust point located at around 80% of the blade's radius. These adjustments in thrust at the blade tips are distinct from the time-averaged analysis discussed previously, as the decrease and increase in thrust are symmetrical and, therefore, do not influence the propeller's time-averaged performance. However, this pattern is connected to the unsteadiness generated between the propellers, which is crucial for noise generation.

VI. Acoustic analysis

In Figure 9(a), S_{pp} is computed by means of the FW-H impermeable formulation discussed in Section III for one microphone located at $X = -10D$ and $Y = Z = 0$, i.e., upstream of the middle propeller. The far-field sound spectrum obtained from the middle propeller of the case with $\Delta\phi = 0°$ is compared with that obtained from the isolated propeller.

Three tonal peaks are present in the case with $\Delta\phi = 0°$, at the first BPF and harmonics. These tones are attributed to the unsteadiness generated by the aerodynamic tip-on-tip interaction discussed in Section V and dominate the acoustic emissions at microphone location. In contrast, the isolated-propeller case presents a sound spectrum without any tonal peaks that stand out visibly from the average broadband level identified by the simulation. This is because the amplitude of steady loading noise and thickness noise is maximum in the plane of the rotor and minimum along the propeller axis, as explained in Section IV. Keeping in mind that the focus of this work is on tonal noise, we ensured that the amplitude of the tonal peaks at the first and second BPFs does not change when the length of the temporal signal, on which the sound spectrum is calculated, is varied. In Figure 9(b), we compare the isolated-propeller case versus the

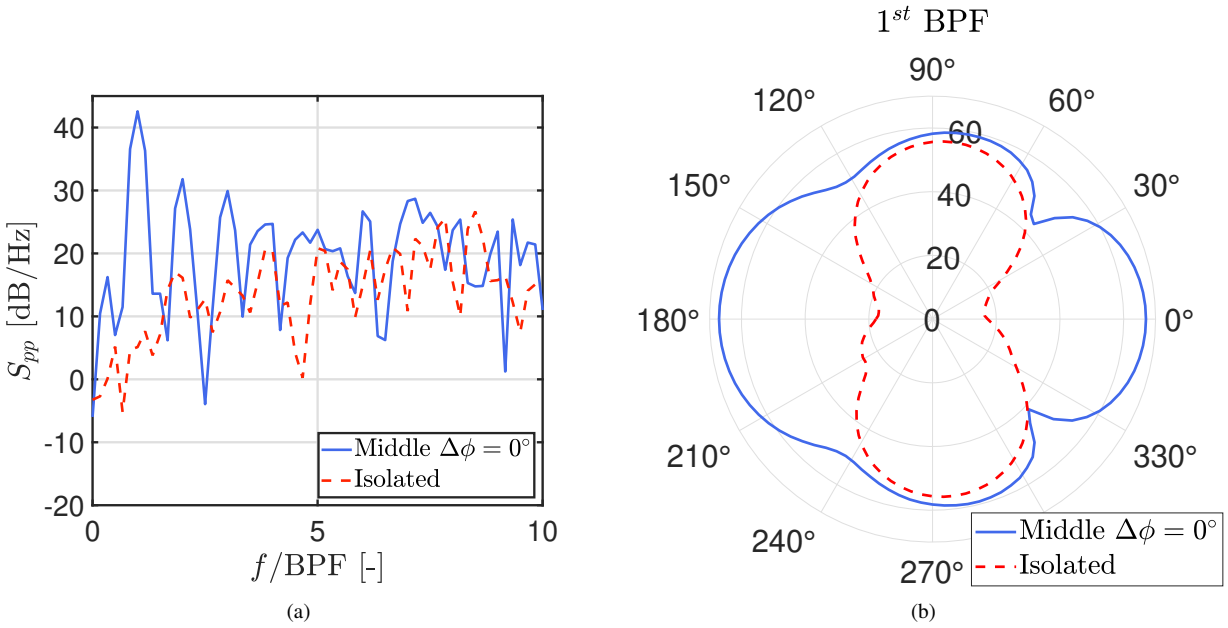

Fig. 9 (a) Far-field noise power spectral density S_{pp} , with microphone position at $X = -10D$ and $Y = Z = 0$; comparison between the distributed middle propeller with $\Delta\phi = 0°$ against the isolated one. (b) Far-field sound L_p directivity plot comparing the distributed middle propeller with $\Delta\phi = 0°$ and the isolated one.

middle-propeller case when $\Delta\phi = 0°$. We illustrate how the sound pressure level L_p varies in the XY plane with the microphones placed $10D$ from the GRS origin in Figure 1(b). We can see that at 90°, the middle propeller generates sound emissions that exceed the one generated by the isolated propeller by about 2.5 dB. This is attributed to the larger level of flow unsteadiness induced by the proximity of the side propellers. The horizontal directivity lobes that strongly dominate the upstream and downstream directions of the flow are also due to this interaction. As a consequence, we infer that the unsteady loading interaction between adjacent rotors is by far the dominant generating mechanism for this DP configuration, especially upstream and downstream of the propellers.

In Figure 10(a), we show the effect of employing a different relative phase angle $\Delta\phi$, comparing the tone generated at the first BPF by the middle propeller for the configuration with $\Delta\phi = 0°$ versus the one for the configuration with $\Delta\phi = 15°$. We may observe that generally, the shape of the sound directivity remains very similar between the two cases. However, the case with $\Delta\phi = 15°$ exhibits less noise amplitude in the direction of the axis of rotation by 4.2 dB. This can be explained by the reduced aerodynamic interaction between propellers that occurs in this case, as demonstrated earlier in Figure 6(b). Differently, in the rotor plane, since steady loading noise dominates the sound emission and since the difference in average thrust between the two cases is negligible, we obtain almost the same level of sound emission along this direction. In Figure 10(b), the comparison of the tone at the second BPF for the two DP configurations is depicted. Again, the shape of the directivity lobes is quite similar between the two examined cases. However, the configuration with $\Delta\phi = 0°$ shows higher noise amplitude in all the directions (about 7 dB along the rotation axis direction). This is also caused by the unsteady loading interactions, according to the propeller noise theory [32].

In Figure 11(a), we show the directivity plot obtained by accounting for the three propellers. This is in order to identify whether acoustic interference between the three propellers would significantly change the sound directivity of the tone at the first BPF. However, this does not occur since it retains essentially the same shape of the sound lobes as in the case of Figure 10(a), where only the middle-propeller contribution was included. Similarly, this also occurs in Figure 11(b), where the tonal directivity at the second BPF is depicted. One might expect that there would be other acoustic interaction effects that would change the directivity shape at the first BPF, but this is not the case since the acoustic wavelengths corresponding to the first and second BPFs are large compared to the characteristic distance between the sound sources on the blade or on the blade tips of two adjacent rotors. These frequencies are therefore acoustically compact and the sound directivity maintains a shape similar to that of the isolated rotor. Hence, it is the unsteady tip-on-tip interaction that determines the sound-emission directivity around the propeller array. However, we

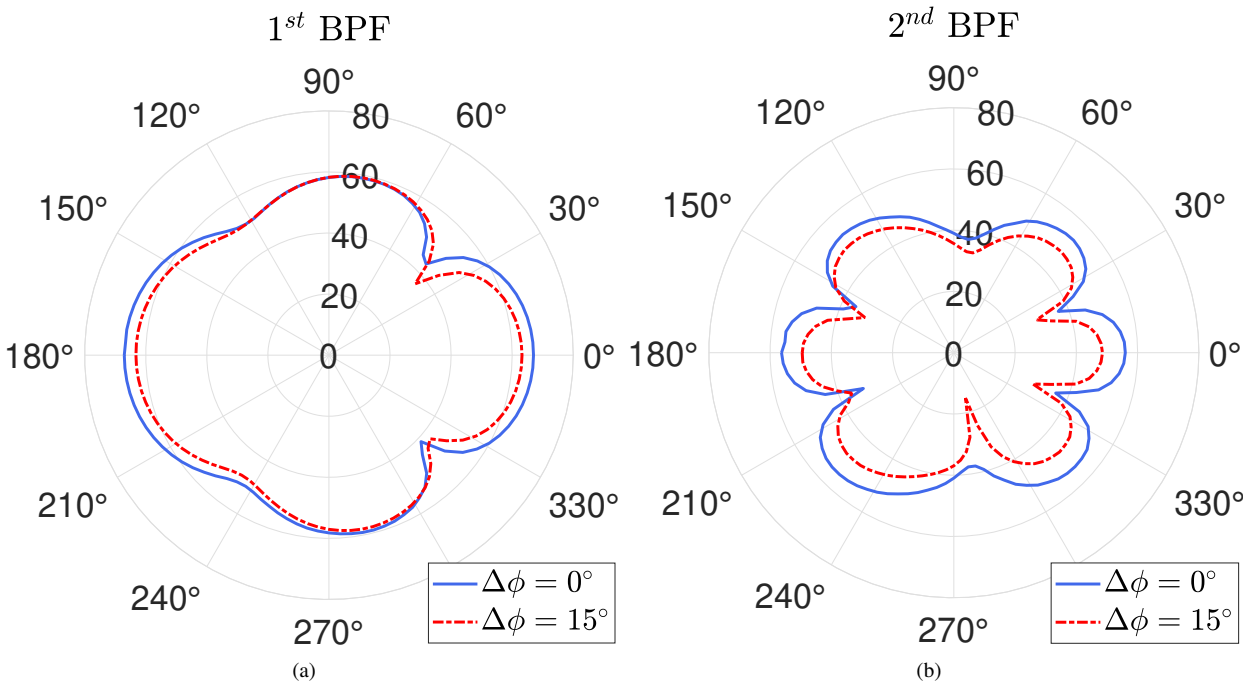

Fig. 10 Far-field sound L_p directivity plot comparing the distributed middle propellers with $\Delta\phi = 0°$ and $\Delta\phi = 15°$. Tones at the first BPF (a), and at the second BPF (b).

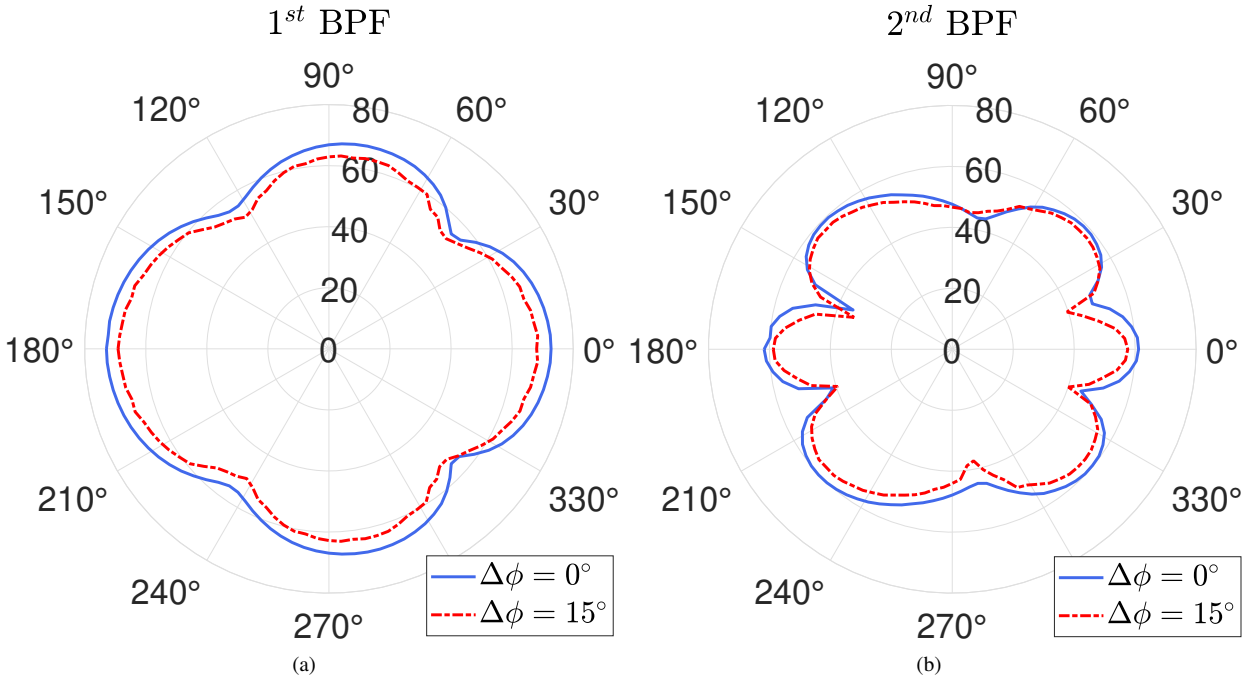

Fig. 11 Far-field sound L_p directivity plot obtained summing the 3 propellers contributions for the 2 analyzed configurations with $\Delta\phi = 0°$ and $\Delta\phi = 15°$. Tones at the first BPF (a), and at the second BPF (b).

remark that along the vertical direction the case with $\Delta\phi = 0°$ radiates about 4 dB more than the one with $\Delta\phi = 15°$. We conjecture that this amplification effect may be due to an acoustic constructive/destructive interference, caused by the

relative phase angle $\Delta\phi$. To prove that, we report the acoustic pressure signal as a function of time at the microphone location $Y = -10D$, $X = Z = 0$ for the DP case with $\Delta\phi = 0°$ in Figure 12(a). This is computed removing the mean of the pressure signal $\bar{p}$ as $p' = p - \bar{p}$. We notice that the acoustic pressure signals computed from the three propellers are in phase. Differently, observing the DP case with $\Delta\phi = 15°$, the middle-propeller acoustic pressure signal shows a time

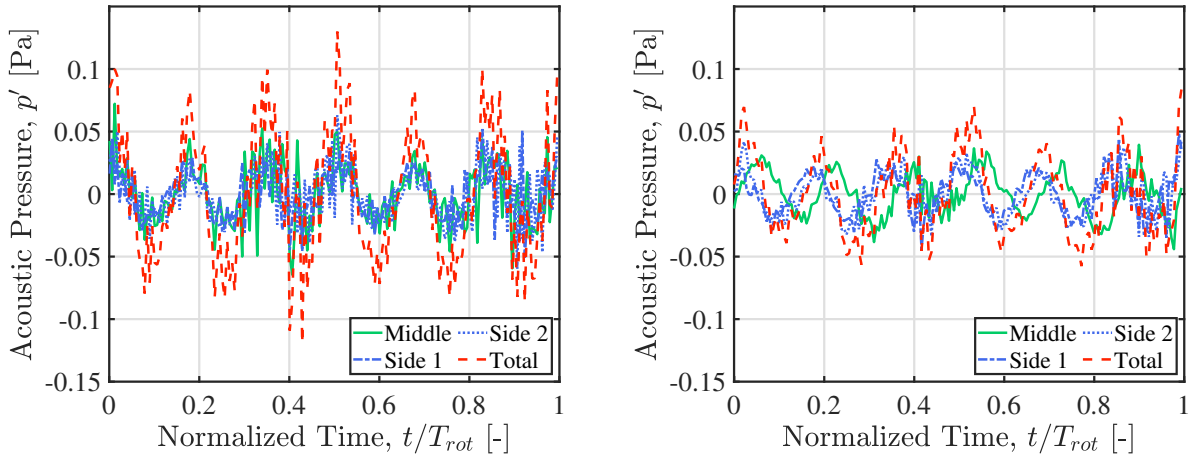

Fig. 12 Acoustic pressure signal as a function of time at microphone location $Y = -10D$, $X = Z = 0$; in (a) the DP case with $\Delta\phi = 0°$ is depicted, in (b) the DP case with $\Delta\phi = 15°$.

shift which leads to a destructive acoustic interference that mitigate the total radiated noise along this direction.

VII. Conclusions

This manuscript presents a numerical investigation of the aerodynamic interaction between adjacent propellers in forward flight, aimed at addressing the gaps in knowledge regarding this interaction as highlighted in Ref. [13]. The 3DS PowerFLOW software is used to calculate the flow field, while an impermeable FW-H formulation present within the solver PowerACOUSTICS was used to obtain the acoustic data.

The results indicate that, when subject to the presence of adjacent propellers, the helical vortical structures generated at the tip of the blades do not break down but deform. This confirms the experimental observations. The deformations modify the downstream wake of the propeller, leading to a loss of azimuthal uniformity. Furthermore, the presence of adjacent propellers amplifies the unsteadiness of the thrust profile, which increases the sound emissions. This effect is most pronounced along the propeller rotation axis, where amplifications above 50 dB are observed. Thus, the dominant sound-generating mechanism in this distributed propulsion configuration is loading noise, especially its unsteady part due to the close interaction between the tips of adjacent blades.

The impact of the relative phase angle on aerodynamic performance is negligible, resulting in a change in thrust coefficient of less than 0.75%. However, findings reveal a reduction in the unsteady thrust profile when a non-zero $\Delta\phi$ is introduced, leading to a mitigation of the unsteady loading noise on the rotation axis and at the first BPF of 4.2 dB. This effect is attributed to the impulsive interaction between adjacent rotors described in Ref. [13] and cannot be characterized in a time-averaged sense since it depends directly on the local azimuthal and radial variation of the blade load. In addition, the relative phase angle produces a constructive/destructive acoustic interference effect when analyzing the noise emitted simultaneously from the array of the three propellers.

Several questions still remain to be answered in future work. First of all it would be interesting to understand how the unsteady aerodynamic mitigation varies for cases in which $\Delta\phi$ differs from those examined, for example by confirming the mitigation trend when the relative phase angle reaches the maximum with $\Delta\phi = 30°$. As the tip-on-tip interaction has been found to possess an unsteady nature, conventional low-order steady-state models, such as vortex tube wake models, cannot be utilized during the design phase to model the noise variations that result from the relative phase angle. Therefore, an alternative method that accounts for this angle should be considered. Additionally, it is worth investigating

whether the presence of neighboring propellers affects the broadband noise, or if the noise can be analyzed separately from the isolated-propeller case.

Acknowledgments

The X-PROP-S CAD model utilized in the simulations was made available by the Delft University of Technology (Netherlands), and the authors express their gratitude for this contribution. In addition, the authors would like to thank Mr. Jatinder Goyal for his support in developing the numerical simulations.

This project has received funding from the European Union's Horizon 2020 research and innovation programme under grant agreement No 860103.

References

[1] European Commission and Directorate-General for Mobility and Transport and Directorate-General for Research and Innovation, Flightpath 2050: Europe's vision for aviation: maintaining global leadership and serving society's needs, Publications Office, 2011. https://doi.org/doi/10.2777/50266.

[2] NASA, "Strategic Implementation Plan: 2017 Update," https://www.nasa.gov/sites/default/files/atoms/files/sip-2017-03-23-17-high.pdf, Washington, DC, 2017.

[3] Borer, N. K., Patterson, M. D., Viken, J. K., Moore, M. D., Bevirt, J., Stoll, A. M., and Gibson, A. R., "Design and Performance of the NASA SCEPTOR Distributed Electric Propulsion Flight Demonstrator," 16th AIAA Aviation Technology, Integration, and Operations Conference, American Institute of Aeronautics and Astronautics, 2016. https://doi.org/10.2514/6.2016-3920, URL https://arc.aiaa.org/doi/10.2514/6.2016-3920.

[4] Stoll, A. M., Stilson, E. V., Bevirt, J., and Pei, P. P., "Conceptual Design of the Joby S2 Electric VTOL PAV," 14th AIAA Aviation Technology, Integration, and Operations Conference, American Institute of Aeronautics and Astronautics, 2014. https://doi.org/10.2514/6.2014-2407, URL https://arc.aiaa.org/doi/10.2514/6.2014-2407.

[5] Alvarez, E. J., and Ning, A., "Modeling Multirotor Aerodynamic Interactions Through the Vortex Particle Method," American Institute of Aeronautics and Astronautics, 2019. https://doi.org/10.2514/6.2019-2827, URL https://arc.aiaa.org/doi/10.2514/6.2019-2827.

[6] Kim, H. D., Perry, A. T., and Ansell, P. J., "A review of distributed electric propulsion concepts for air vehicle technology," 2018 AIAA/IEEE Electric Aircraft Technologies Symposium (EATS), IEEE, 2018, pp. 1–21.

[7] Kummer, J., and Dang, T., "High-Lift Propulsive Airfoil with Integrated Crossflow Fan," Journal of Aircraft, Vol. 43, 2006, pp. 1059–1068. https://doi.org/10.2514/1.17610.

[8] Teets, E. H. J., Donohue, C. J., and Wright, P. T., "Meteorological Support of the Helios World Record High Altitude Flight to 96,863 Feet," 2002, p. 22.

[9] Zhou, W., Ning, Z., Li, H., and Hu, H., "An Experimental Investigation on Rotor-to-Rotor Interactions of Small UAV Propellers," 35th AIAA Applied Aerodynamics Conference, American Institute of Aeronautics and Astronautics, 2017. https://doi.org/10.2514/6.2017-3744.

[10] Alvarez, E., Schenk, A., Critchfield, T., and Ning, A., "Rotor-on-Rotor Aeroacoustic Interactions of Multirotor in Hover," Vol. 4053, Brigham Young University Faculty Publications, 2020, p. 13.

[11] Lee, H., and Lee, D.-J., "Rotor interactional effects on aerodynamic and noise characteristics of a small multirotor unmanned aerial vehicle," Vol. 32, No. 4, Physics of Fluids, 2020. https://doi.org/10.1063/5.0003992.

[12] Zarri, A., Dell'Erba, E., Munters, W., and Schram, C., "Aeroacoustic installation effects in multi-rotorcraft: Numerical investigations of a small-size drone model," Vol. 128, Aerospace Science and Technology Journal, 2022, p. 107762. https://doi.org/10.1016/j.ast.2022.107762, URL https://linkinghub.elsevier.com/retrieve/pii/S1270963822004369.

[13] de Vries, R., van Arnhem, N., Sinnige, T., Vos, R., and Veldhuis, L. L., "Aerodynamic interaction between propellers of a distributed-propulsion system in forward flight," Aerospace Science and Technology, Vol. 118, 2021, p. 107009. https://doi.org/10.1016/j.ast.2021.107009, URL https://linkinghub.elsevier.com/retrieve/pii/S1270963821005198.

[14] Zarri, A., Dell'Erba, W., Edoardo Munters, and Schram, C., "Fuselage scattering effects in a hovering quadcopter drone," 28th AIAA/CEAS Aeroacoustics 2022 Conference, American Institute of Aeronautics and Astronautics, 2022. https://doi.org/10.2514/6.2022-3031, URL https://arc.aiaa.org/doi/10.2514/6.2022-3031.

[15] Zarri, A., Christophe, J., Moreau, S., and Schram, C., "Influence of Swept Blades on Low-Order Acoustic Prediction for Axial Fans," Acoustics, Vol. 2, No. 4, 2020, pp. 812–832. https://doi.org/10.3390/acoustics2040046, URL https://www.mdpi.com/2624-599X/2/4/46.

[16] Torija, A. J., and Clark, C., "A Psychoacoustic Approach to Building Knowledge about Human Response to Noise of Unmanned Aerial Vehicles," International Journal of Environmental Research and Public Health, Vol. 18, No. 2, 2021. URL https://www.mdpi.com/1660-4601/18/2/682.

[17] Roger, M., "On Combined Propeller Synchronization And Edge Scattering For The Noise Reduction Of Distributed Propulsion Systems," ICSV26, Montreal, 2019, p. 8.

[18] Pascioni, K. A., Rizzi, S. A., and Schiller, N., "Noise Reduction Potential of Phase Control for Distributed Propulsion Vehicles," American Institute of Aeronautics and Astronautics, 2019. https://doi.org/10.2514/6.2019-1069, URL https://arc.aiaa.org/doi/10.2514/6.2019-1069.

[19] Zhou, T., and Fattah, R., "Tonal Noise Acoustic Interaction Characteristics of Multi-Rotor Vehicles," American Institute of Aeronautics and Astronautics, 2017. https://doi.org/10.2514/6.2017-4054, URL https://arc.aiaa.org/doi/10.2514/6.2017-4054.

[20] Patterson, A., Schiller, N. H., Ackerman, K. A., Gahlawat, A., Gregory, I. M., and Hovakimyan, N., "Controller Design for Propeller Phase Synchronization with Aeroacoustic Performance Metrics," American Institute of Aeronautics and Astronautics, 2020. https://doi.org/10.2514/6.2020-1494, URL https://arc.aiaa.org/doi/10.2514/6.2020-1494.

[21] Avallone, F., Casalino, D., and Ragni, D., "Impingement of a propeller-slipstream on a leading edge with a flow-permeable insert: A computational aeroacoustic study," Vol. 17, No. 6, 2018, pp. 687–711. https://doi.org/10.1177/1475472X18788961, URL http://journals.sagepub.com/doi/10.1177/1475472X18788961.

[22] Romani, G., Grande, E., Avallone, F., Ragni, D., and Casalino, D., "Performance and noise prediction of low-Reynolds number propellers using the Lattice-Boltzmann method," Vol. 125, 2022, p. 107086. https://doi.org/10.1016/j.ast.2021.107086, URL https://linkinghub.elsevier.com/retrieve/pii/S1270963821005964.

[23] Casalino, D., Romani, G., Zhang, R., and Chen, H., "Lattice-Boltzmann Calculations of Rotor Aeroacoustics in Transitional Boundary Layer Regime," American Institute of Aeronautics and Astronautics, 2022. https://doi.org/10.2514/6.2022-2862, URL https://arc.aiaa.org/doi/10.2514/6.2022-2862.

[24] Bhatnagar, P. L., Gross, E. P., and Krook, M., "A Model for Collision Processes in Gases. I. Small Amplitude Processes in Charged and Neutral One-Component Systems," Phys. Rev., Vol. 94, 1954, pp. 511–525. https://doi.org/10.1103/PhysRev.94.511, URL https://link.aps.org/doi/10.1103/PhysRev.94.511.

[25] Shan, X., and Chen, H., "Kinetic theory representation of hydrodynamics: A way beyond the Navier-Stokes equation," Journal of Fluid Mechanics, Vol. 550, 2006, pp. 413 – 441. https://doi.org/10.1017/S0022112005008153.

[26] Nie, X., Shan, X., and Chen, H., A Lattice-Boltzmann / Finite-Difference Hybrid Simulation of Transonic Flow, 2009. https://doi.org/10.2514/6.2009-139, URL https://arc.aiaa.org/doi/abs/10.2514/6.2009-139.

[27] Chen, H., Teixeira, C., and Molvig, K., "Realization of Fluid Boundary Conditions via Discrete Boltzmann Dynamics," International Journal of Modern Physics C, Vol. 09, 1998, pp. 1281–1292.

[28] Yakhot, V., and Orszag, S. A., "Renormalization-Group Analysis of Turbulence," Phys. Rev. Lett., Vol. 57, 1986, pp. 1722–1724. https://doi.org/10.1103/PhysRevLett.57.1722, URL https://link.aps.org/doi/10.1103/PhysRevLett.57.1722.

[29] Romani, G., and Casalino, D., "Rotorcraft blade-vortex interaction noise prediction using the Lattice-Boltzmann method," Aerospace Science and Technology, Vol. 88, 2019, pp. 147–157. https://doi.org/https://doi.org/10.1016/j.ast.2019.03.029, URL https://www.sciencedirect.com/science/article/pii/S1270963818321011.

[30] Farassat, F., "Derivation of Formulations 1 and 1A of Farassat," 2007.

[31] Casalino, D., "An advanced time approach for acoustic analogy predictions," J. Sound Vib., Vol. 261, 2003, pp. 583–612. https://doi.org/10.1016/S0022-460X(02)00986-0.

[32] Goldstein, M. E., Aeroacoustics, 1976.

[33] Glegg, S., and Devenport, W., Aeroacoustics of low mach number flows: Fundamentals, analysis, and measurement, 2017.

[34] Romani, G., Grande, E., Avallone, F., Ragni, D., and Casalino, D., "Performance and noise prediction of low-Reynolds number propellers using the Lattice-Boltzmann method," Aerospace Science and Technology, 2021, p. 107086. https://doi.org/https://doi.org/10.1016/j.ast.2021.107086, URL https://www.sciencedirect.com/science/article/pii/S1270963821005964.

[35] Casalino, D., Grande, E., Romani, G., Ragni, D., and Avallone, F., "Definition of a benchmark for low Reynolds number propeller aeroacoustics," Aerospace Science and Technology, Vol. 113, 2021, p. 106707. https://doi.org/https://doi.org/10.1016/j.ast.2021.106707, URL https://www.sciencedirect.com/science/article/pii/S1270963821002170.

[36] Casalino, D., Avallone, F., Gonzalez-Martino, I., and Ragni, D., "Aeroacoustic study of a wavy stator leading edge in a realistic fan/OGV stage," Journal of Sound and Vibration, Vol. 442, 2019, pp. 138–154. https://doi.org/https://doi.org/10.1016/j.jsv.2018.10.057.

[37] Grande, E., Ragni, D., Avallone, F., and Casalino, D., "Laminar Separation Bubble Noise on a Propeller Operating at Low Reynolds Numbers," AIAA Journal, Vol. 60, 2022, pp. 5324–5335. https://doi.org/https://doi.org/10.2514/6.2018-2952.

[38] Casalino, D., Barbarino, M., and Visingardi, A., "Simulation of Helicopter Community Noise in Complex Urban Geometry," AIAA Journal, Vol. 48, No. 8, 2011, pp. 1614–1624.